Ferdowsi University of Mashhad

Journal of Applied and Computational Sciences in Mechanics

Page Journal: mechanic-ferdowsi.um.ac.ir

Society of Manufacturing Engineering of Iran

Influence of Cooling Rate on Hardness and Machinability in Low-Carbon Steel WAAM

Mohammad Ebadi Tavallaei[1], Kiana Arteshyar[2], Mahdi Mazloom Farsibaf[3], Farhad Kolahan[4], Sadegh Elhami[5]

10.22067/jacsm.2026.93580.1329

Wire Arc Additive Manufacturing (WAAM), especially in its Metal Active Gas (MAG) form, has emerged as a promising technique for fabricating large and complex metal components. In this study, walls were built on ST37 steel substrates using ER70S-6 filler wire, with voltage and travel speed varied between 20–22 V and 100–200 mm/min, respectively. Hardness measurements revealed a gradient from 213.5 HV at the edges to 137.4 HV at the center, attributed to differing cooling rates. Rapid edge cooling led to fine-grained microstructures, while slower cooling in the center resulted in coarser grains. Optical microscopy confirmed a hypoeutectoid microstructure of ferrite and pearlite. Despite minor porosity, the produced walls showed a yield strength of 490 MPa, significantly higher than the 400 MPa of the base metal. These findings demonstrate the mechanical effectiveness of the WAAM-MAG process. However, the non-uniform hardness can impact machining performance, making tool selection and parameter optimization essential. Accurate assessment of hardness gradients is crucial for improving post-processing and achieving consistent component quality.

***Keywords*: Wire Arc Additive Manufacturing, Hardness Distribution, Microstructural and Mechanical Analysis, Low-carbon steel alloy, ER70S-6 wire filler.**

I. Introduction

Advancements in technology and the increasing demand for producing complex and efficient components have led to a shift from traditional manufacturing methods to innovative techniques like Additive Manufacturing (AM). Moreover, AM minimizes additional processing steps and waste associated with production, particularly in customized or low-volume production. One of the key indicators for evaluating the efficiency of this method compared to conventional methods is the Buy-to-Fly Ratio (BTF ratio). This ratio represents the amount of raw material needed to produce each unit of finished product [1], and optimizing it can help reduce costs, enhance process efficiency, and make it more environmentally friendly and is recognized as an innovative and optimized solution across many industries [2, 3]. Three-dimensional printing (3D printing), also known as AM, has transformed the manufacturing industry through its ability to create complex objects with high precision by adding material layer by layer [4]. Initially, 3D printing was primarily used for prototyping and conceptual modeling, but advancements in technology have expanded its applications to the production of final components in various industries. AM involves building parts directly from raw materials, often using high-energy beams such as lasers or electron beams [5]. For metals, AM techniques are categorized into methods like powder bed fusion (PBF), directed energy deposition (DED), material extrusion, and sheet lamination [4]. Each category includes different technologies made by various manufacturers. These methods offer diverse capabilities, enabling the production of intricate and functional parts across multiple domains. Among these techniques, PBF and DED are particularly significant for metal additive manufacturing (MAM) [4]. The variations in energy sources, process settings, and cooling rates in MAM significantly impact the shape and size of the melt pool. These differences in melt pool geometry play a crucial role in shaping the microstructures of the final product, ultimately affecting mechanical properties [6]. PBF is a 3D printing process that uses powder as the raw material to create parts. In this technique, metal or plastic powder is evenly spread in a thin layer on a horizontal surface. A heat source, such as a laser or electron beam, precisely melts the surface of the

* Manuscript received May 18, 2025, Revised October 08, 2025, Accepted February 03, 2026.

[1] MSc.Mechanical Engineering Department, Ferdowsi University of Mashhad, Mashhad, Razavi Khorasan, Iran.

[2] BSc.Mechanical Engineering Department, Ferdowsi University of Mashhad, Mashhad, Razavi Khorasan, Iran.

[3] MSc.Mechanical Engineering Department, Ferdowsi University of Mashhad, Mashhad, Razavi Khorasan, Iran.

[4] Corresponding Author. Associate Professor, Mechanical Engineering Department, Ferdowsi University of Mashhad, Mashhad, Razavi Khorasan,Iran. **Email**: kolahan@ferdowsi.um.ac.ir

[5] Assistant professor. Mechanical Engineering Department, Ferdowsi University of Mashhad, Mashhad, Razavi Khorasan, Iran.

layer, causing selected areas of the powder to fuse and form the desired shape. This process continues layer by layer, with new powder added and then melted to build up the final part. One of the main advantages of this technique is its ability to produce parts with complex geometries and fine details that are not easily achievable with conventional manufacturing methods [7]. DED is an AM method that uses focused energy sources, such as lasers, plasma arcs, or electron beams, to melt and deposit materials. In this process, raw materials, typically in the form of powder or wire, are directed into the melt pool, where they are fused and built up progressively to form the final component. DED allows for high precision, material flexibility, and the ability to create both new parts and refurbish existing ones [8]. GMAW (Gas Metal Arc Welding) and GTAW (Gas Tungsten Arc Welding) are categorized under DED. In these methods, an electric arc is used to melt the metallic feedstock. In GMAW, a consumable metal electrode serves as both the filler material and the arc source. This method, due to its high deposition rate and efficiency, is suitable for manufacturing larger and industrial-scale parts [9]. Conversely, GTAW utilizes a non-consumable electrode -usually tungsten- to create the arc, with the filler material added separately. This provides greater control over the process, enabling the production of parts with higher precision and superior surface quality [10, 11]. The shielding gas used plays a crucial role in preventing oxidation and enhancing the quality of the deposited layers, with gases like argon or argon-carbon dioxide mixtures being commonly applied, depending on the material type [12]. In WAAM, GMAW is typically controlled by a robotic arm or a mechanical system to precisely guide the wire into the arc zone, forming molten layers [13]. Accurate adjustment of parameters such as current, arc voltage, and wire feed speed is essential to achieve high quality and minimize defects [14].

The history of research in the WAAM field dates back to the early 2000s, and significant advancements have been made in recent years [13]. J. Vora et al, [15] studied the WAAM process using GMAW on SS316L to build multi-layer structures. They analyzed the microstructure, macrostructure, and mechanical properties, including tensile strength, impact resistance, and microhardness. The results showed that the tensile properties of the samples were within the expected range for SS316L, with ultimate tensile strength (UTS) of 485 MPa, yield strength (YS) of 220 MPa, and elongation of 45%. The multi-layer samples had an average UTS of 512.53 MPa, YS of 256.57 MPa, and elongation of 49.35%, confirming the process produced high-quality parts. Pranjal Shukla et al, [16] examined the effects of correction parameters, namely Arc Length Correction (ALC), Dynamic Correction (DC), and Pulse Correction (PC), on ER70S-6 filler wire deposition on mild steel using Cold Metal Transfer (CMT) and Pulsed mode in the GMAW process. The goal was to control heat input to improve bead quality. Results showed that heat input increased with ALC and decreased with DC and PC. Bead width and penetration increased with heat input, while bead height and microhardness decreased. These findings offer flexibility and consistency for advanced welding and WAAM applications. Su et al, [17] explored the use of WAAM with CMT technology to fabricate Al-Mg alloys using ER5356 wire, focusing on how heat input (via wire feed speed and travel speed) affected the microstructure and mechanical properties. The results revealed that grain size varied with different processing conditions, and the main phases present were α-phase (Al) and β-phase (Al3Mg2). Mechanical properties, including microhardness (70-77 Hv), UTS 255 MPa, yield strength (128 MPa), and elongation (23.2%), remained stable across various conditions. The study concluded that WAAM-CMT-manufactured parts performed better than conventional 5356 casting alloys. Tongov et al, [18] examined WAAM using G3Si1 wire to evaluate the impact of heat input and interlayer temperature on mechanical properties. Microstructure and microhardness analyses revealed that thermal treatment from subsequent layers affected the microstructure along the sample height, except in the final layer. Heat input and interlayer temperature were identified as key factors influencing the mechanical characteristics. Nagallapati et al, [19] examined passive and active thermal management approaches to reduce residual stresses and distortion in AM process of metal components (EN8 and ER70S-6). The results showed that active thermal management reduced distortion by 65% (from 1.226 mm to 0.431 mm) and residual stresses by 49% (from 492.31 MPa to 250.68 MPa). With active heating, distortion decreased by 63% (from 1.35 mm to 0.50 mm). The study highlighted that substrate heating is effective in managing distortion and improving mechanical properties. Fan et al, [20] aimed to reduce residual stresses and refine coarse grains in WAAM by using trailing cooling with argon gas. The results showed that applying cooled gas reduced longitudinal stress and improved dimensional accuracy, with maximum joint displacement decreasing by 24%. Additionally, the grain size of the deposited metal was refined, increasing tensile strength by 10% and elongation by 8%. The study demonstrated the effectiveness of trailing cooling in improving both the mechanical properties and accuracy of WAAM components. Panicker et al, [21] examined the impact of thermal phenomena in WAAM on the microstructure and mechanical properties of G4Si1 and AM70 steels. Results showed that fine grains formed at higher temperatures, while coarser grains developed as part height increased. Hardness decreased with height, and lower energy input improved hardness and yield strength but reduced elongation. The findings highlight the importance of controlling thermal effects to optimize WAAM part properties. Wildenhain et al, [22] focused on welding stresses and cold cracking risks in WAAM of high-strength steels using a high-strength filler metal (yield strength >790 MPa). The specimens were welded with controlled heat input (200–650 kJ/m) and interlayer temperatures (100–300 °C). Results showed that higher heat input reduced tensile stress but worsened microstructure and mechanical properties, while lower interlayer temperatures improved properties and reduced stress. Component design influenced heat dissipation and residual stress. The study aimed to develop practical guidelines for safe and efficient WAAM of high-strength steels.

Dornelas et al, [23] developed a μ-GMA prototype for downscaled direct energy deposition (μ-DED) using micrometric wires. The prototype deposited beads with an approximate width of 1 mm, nearly 5 times thinner than standard GMA-based DED, with a build rate of 30 cm^3/h. The mechanical properties of the μ-GMA deposits were comparable to those of regular GMA-based DED parts.

This study aims to investigate the metallurgical and mechanical properties of the fabricated walls, particularly at the edges of the walls, as these properties may differ from those of the core. This issue is especially significant for post-processing operations such as machining and milling, as understanding these properties is essential for determining appropriate parameters for these processes. One of the most important machining parameters is feed, making it crucial to understand how the hardness varies from the wall to the core and how the hardness profile changes across these regions. To achieve this objective, it is necessary to measure the hardness of the walls in various sections of the samples. Post-processing requires a deeper investigation into some mechanical and metallurgical aspects of the fabricated walls to select proper machining parameters, which represents a gap in other literature. To fill this gap, this research was conducted to create a hardness profile and examine variations in hardness across different parts of the walls. Additionally, one of the key applications of WAAM is in the manufacturing of medical implants, where both hardness and surface quality play a critical role in the implant's success and integration with surrounding biological tissues. Research has demonstrated that surface roughness significantly influences osteoblast adhesion, which directly impacts osseointegration, the process by which bone tissue fuses with the implant. Optimized surface roughness enhances cellular attachment and accelerates integration, contributing to improved implant stability and long-term success [24]. However, excessively high hardness can lead to mismatches in the elastic modulus between the implant and surrounding bone. This discrepancy may cause stress shielding, where the implant absorbs a greater share of mechanical loads, reducing the natural stimulation required for bone regeneration. Over time, this can result in localized bone resorption and implant failure [25]. Therefore, achieving an optimal balance between hardness and surface properties is essential. Studies indicate that a moderate surface roughness within the range of 1.0 to 2.0 µm provides the best results in terms of cell adhesion and bone integration [26]. Additionally, the optimal hardness for implants should be close to that of natural bone to prevent excessive stress concentrations. Research suggests that a Vickers hardness between 200 and 250 is ideal, as it ensures sufficient mechanical strength while maintaining compatibility with bone tissue [25]. As a result, precision control over the machining process of WAAM-produced implants is crucial. Precise control of machining parameters is critical to achieving an optimal balance between surface roughness and hardness, both of which govern the mechanical stability and biological performance of WAAM-produced implants. Insufficient removal of softer surface layers may hinder osseointegration due to inadequate roughness, while excessive machining can degrade mechanical strength by lowering hardness. In this study, MAG-WAAM was employed to fabricate samples using ER70S-6 filler material, with a focus on correlating key input parameters, travel speed, and welding voltage with the resulting hardness distribution. This understanding is essential for optimizing post-processing strategies, particularly in biomedical applications where surface and mechanical properties are tightly linked to implant success. Although an economical filler material (ER70S-6) was selected due to budgetary constraints, the developed methodology is readily transferable to high-performance alloys such as Inconel. Consequently, the findings offer a scalable framework for process optimization across critical sectors, including aerospace and biomedical manufacturing. In summary, the present research aims to establish a comprehensive correlation between process parameters, cooling rate, and hardness evolution within MAG-WAAM fabricated low-carbon steel walls. By quantifying hardness gradients and linking them to microstructural transformations, this work provides practical guidance for optimizing machining conditions and improving the reliability and surface integrity of WAAM-fabricated components in both industrial and biomedical applications.

II. MATERIALS AND METHODS

This section outlines the materials, equipment, and experimental procedures used in the WAAM process. The methodology is divided into several subsections covering material selection, process parameters, testing methods, and microstructural analysis.

A. Materials

In this study, ER70S-6 filler wire with a diameter of 1.2 mm was used for the WAAM process and wall construction. ER70S-6 is a low-carbon steel alloy widely used due to its excellent weldability, ready availability, and low cost. It is especially suitable for joining carbon and low-alloy steel [27]. ST37 steel plates, with dimensions of 100 mm × 200 mm × 6 mm, were selected as the substrate for constructing the walls due to their high weldability. The chemical composition and mechanical properties of the ER70S-6 filler are presented in Tables 1 and 2, respectively.

Table 1- Chemical composition of the wire (ER70S-6) [49]

Element	**C**	**Mn**	**Si**	**P**	**Mo**	**Cr**	**Ni**	**Cu**	**V**
weight percent	0.09	<1.60	0.9	0.007	0.05	0.05	0.05	0.2	0.05

Table 2- Mechanical properties of the wire (ER70S-6) [45]

Property	**Wire (ER70S-6)**
Tensile Strength	483- 827 MPa
Yield Strength	≥ 400 MPa
Elongation	≥ 20%
Hardness (Brinell)	Not typically specified
Impact Toughness	Varies by grade; 27 J at -30 °C

B. Experimental Design and Equipment Setup

The experiments were conducted using a full factorial design matrix to systematically explore the process parameters for the WAAM procedure. The use of a full factorial design and Design-Expert 12 software offers high accuracy and identifies interactions between variables [28].

The welding operations utilized the PARS MIG-SP501 inverter machine by Gam Electric Company and were conducted on a dual-axis workbench designed to enhance precision and control. The workbench facilitated linear movement in the left-right direction for horizontal positioning and vertical adjustment of the welding torch through a power transfer screw, enabling fine control over torch height during the process. A distinct back-and-forth cladding method was employed, where the welding torch moved alternately from left to right and then from right to left on each pass, ensuring even heat distribution, minimized distortion, and consistent cladding layer thickness. This motion strategy was repeated for 15 passes to construct a wall with a final height of approximately 20 mm. Incremental vertical adjustments of the torch with each pass ensured uniformity and precision, with the dual-axis workbench setup playing a key role in achieving the weld's overall accuracy and quality. The equipment used in the welding and wall fabrication section is shown in Fig. 1.

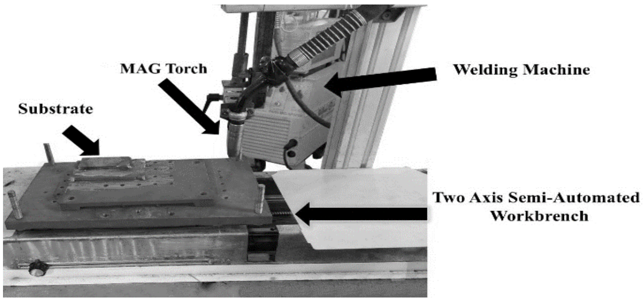

Fig. 1. MAG-WAAM equipment for wall fabrication

C. Process Parameters and Experimental Conditions

To identify the parameters influencing the weld geometry, a series of screening experiments was performed, in which key machine parameters such as voltage and travel speed were systematically varied. The experimental design followed a full factorial approach to investigate the effects of two primary factors, each examined at three different levels. Throughout all experiments, the interlayer temperature was carefully controlled and maintained at approximately 150 °C, monitored using an infrared thermometer (Mastech MS6522B). The selection of this temperature was based on the findings of Fan et al. [29], who reported that maintaining around 150 °C provides an optimal balance between grain refinement and thermal stress control in low-carbon steels. Lower interlayer temperatures (< 100 °C) increase cooling rates excessively and promote brittle microstructures, whereas higher temperatures (> 200 °C) lead to grain coarsening and reduced hardness. Thus, 150 °C was adopted as a critical threshold to ensure refined ferrite–pearlite microstructures and prevent excessive heat accumulation during multilayer deposition. For consistency and accuracy, all measurements, particularly hardness and microstructural evaluations, were conducted along the centerline of the deposited weld bead in each specimen. Other process parameters were held constant to ensure experimental reliability. The complete set of input parameters employed for the MAG-based WAAM process is shown in Table 3.

Table 3- MAG-based WAAM input parameters

Substrate	ST37
Wire filler	ER70S-6
Process	GMAW
Electrode diameter	1.2 mm
Shielding gas	100% CO_2
Travel speed	100,150,200 mm/min
Voltage	20, 21, 22 V
Gap	4 mm
Tip angle of the electrode	90 degree
The angle of the welding torch	90 degree
Gas flow rate	13 L/min
Inter-layer temperature	150 ©

D. Sample Preparation and Tensile Testing

After the walls were fabricated, samples were prepared using the wire-cut process. These samples included cross-sectional specimens for hardness testing and microstructure analysis, as well as tensile specimens. The tensile specimens were prepared and tested based on the ASTM E8/E8M standard, with a dimensional ratio conforming to the standard. The purpose of the tensile tests was to compare the UTS values resulting from different processing parameters. A Santam tensile testing machine was used to perform the tests at a crosshead speed of 0.25 mm/min [30]. It should be noted that all the fabricated samples used for tensile testing were prepared with a consistent cross-sectional area.
According to the findings of Chen et al, [31], the tensile properties obtained in the top, middle, and bottom regions of the multilayer structure showed minimal differences, indicating that the testing location has no significant impact on the results. Although the material in the bottom region exhibited slightly lower strength due to greater heat accumulation, these variations were very small and consistent.

E. Hardness Testing Procedure

To evaluate the hardness distribution across the wall fabricated using the MAG-WAAM process with ER70S-6 welding metal, a comprehensive hardness testing procedure was conducted. To conduct the hardness test, a sample was physically cut from the fabricated walls. The selection was based on specific criteria, primarily maximum build height and tensile strength. According to the full factorial design matrix, Sample No. 3, produced at a voltage of 22 V and a travel speed of 100 mm/min, met these criteria and was selected for testing. The hardness test was performed in accordance with ASTM E384 standards. The selected sample had the highest and lowest weld widths of 8.5 mm and 7.3 mm, respectively. The surface of the selected sample was meticulously prepared to eliminate any scratches or defects that could affect the accuracy of the test results. In the metallography section, the samples were etched according to ASTM E407 and cleaned in an ultrasonic cleaning machine. The Vickers microhardness method was employed to evaluate the hardness distribution in accordance with ASTM E384. In this method, a diamond-shaped pyramid indenter was used to create indentations on the polished surface of the samples. A preliminary test force of 10 grams was applied to accurately position and stabilize the indenter, followed by a main test force of 100 grams, held for a dwell time of 10 seconds. After unloading, the two diagonals of each indentation were measured using an optical microscope. The Vickers hardness number (HV) was then calculated based on the average diagonal length and the applied force, as specified by the standard.

Hardness measurements were performed along three distinct horizontal lines from the base of the weld to the top point of the wall, with 10 points measured on each line. The distance between each horizontal line was 5 mm. To verify measurement repeatability, three independent indentations were performed at each selected line. A horizontal reference line was marked across the polished cross-section of the wall, and indentations were made at three locations: one along the reference line and two others spaced 1 mm above and 1 mm below it. Each indentation was performed by a different operator to minimize human error. The average of the three measured values was taken as the final hardness value for that specific location. Additionally, the standard deviation of the measurements was determined, and error bars were constructed to evaluate the measurement error. The schematic of the hardness testing process on the sample is shown in Fig. 2.

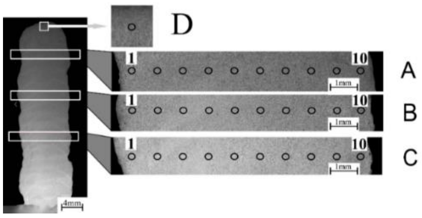

Fig. 2. Schematic of the hardness measurement process along three horizontal lines (A, B, and C) and the highest point on the sample (D)

Following the hardness tests, microstructural and macrostructural images of the samples were captured using an Olympus BX41M optical microscope to further analyze material consistency and properties.

Table 4- Full factorial design matrix and corresponding measured outputs

	Input Parameters		Output Parameters	
Sample Number	Welding Voltage (V)	Travel Speed (mm/min)	Weld Height (mm)	Weld Tensile Strength (MPa)
1	21	100	26.1	410
2	21	150	21.9	493
3	22	100	27.4	490
4	21	200	24.4	425
5	20	100	27.2	449
6	21	150	23.7	512
7	20	150	21.3	503
8	21	150	22.6	509
9	20	200	23.3	397
10	22	200	21.8	453
11	22	150	21.5	516

F. Data Summary and Parameter Matrix

All data are comprehensively summarized in Table 4, which presents all possible combinations of the independent variables, namely travel speed and voltage. This table provides a clear overview of the experimental conditions, allowing for a detailed comparison of their effects on the resulting material properties. Systematically organizing the data facilitates the identification of trends, correlations, and potential interactions between these key parameters.

G. Microstructural Characterization

Before image analysis, the specimens were prepared through standard metallographic procedures. Cross-sections were ground with SiC papers (80 to 2000), polished with diamond paste, and etched with 2% Nital (based on ASTM E8 standard) to reveal ferrite–pearlite structures. Optical microscopy (Olympus BX41M) was used to capture general grain morphology, and SEM imaging provided higher-resolution views of fine features and porosity.

Among all fabricated walls, Sample No. 3 was selected for detailed hardness and microstructural examination. This sample exhibited the maximum wall height (27.4 mm), high tensile strength (490 MPa), reflecting a well-balanced combination of heat input and arc stability. Compared to the other specimens, Sample No. 3 demonstrated the most favorable deposition quality and mechanical performance, representing the optimized processing condition for further analysis. Microscopic imaging was conducted using 200x magnification, focusing on two regions: the center and the edges of the wall, near the hardness measurement points. This analysis provided insight into grain morphology, phase distribution, and potential defects, which were later correlated with the mechanical properties of the sample to evaluate build quality and performance. To establish a reference for evaluating the mechanical behavior of the WAAMed walls, a tensile test was carried out on a specimen extracted from the raw ER70S-6 filler wire. The specimen geometry was identical to that of the WAAM wall tensile samples to ensure a valid comparison. The measured ultimate tensile strength (UTS) of the raw wire was 473 MPa, which is in agreement with values reported in previous studies for cold-drawn ER70S-6 wires of similar diameter [32, 33] where UTS typically ranges between 460-483 MPa. In Fig. 3, the locations of the hardness testing points along one of the horizontal lines are shown. Microhardness profiles along three horizontal lines (A, B and C) across the WAAM wall show a clear, reproducible trend: high hardness at the initial points, pronounced softening toward mid-span, and recovery toward the final points. Quantitatively, profile A decreases from 213.5 HV (point 1) to a minimum of 169.5 HV (point 5) and recovers to 206.6 HV (point 10); profile B falls from 204.1 → 150.6 → 208.7 HV (points 1, 5, 10); profile C is lower overall, 164.3 → 137.4 → 165.7 HV. Error bars are small, indicating the trends exceed experimental scatter. The mid-span softening is attributed to repeated thermal cycling (tempering and grain coarsening), while the end-point hardness recovery likely reflects higher cooling rates or formation of finer hard constituents in the last-deposited layers. The hardness measurements were performed similarly on the other lines as well. Additionally, two microstructural images were captured from the central region and the wall of the specimen, which are shown in images (a) and (b), respectively.

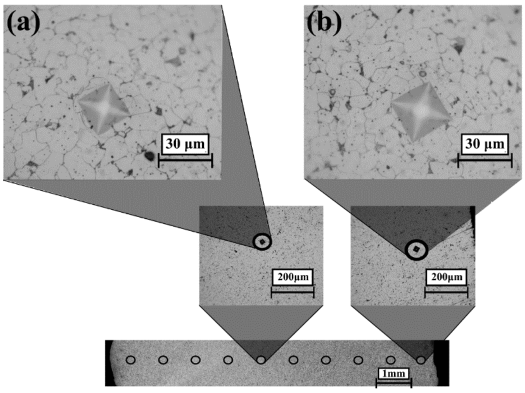

Fig. 3. Hardness testing locations along line B, with corresponding microstructural images of the central region (a) and the wall (b)

H. Image Analysis

To analyze the microstructure, ImageJ software was utilized. This software enables precise image processing and analysis, including grain size measurement, grain counting within a specified area, and grain size distribution assessment [34]. For each microstructural image, a square region with dimensions of 10 mm × 10 mm was extracted from the central area of the image. Within this defined region, the number of grains was counted manually using the grain counting feature of the software. The grain count within this specified area was then used as a qualitative indicator of grain refinement; a higher grain count per unit area corresponds to a finer microstructure. Additionally, grain size distribution and area fraction were assessed to further characterize the microstructural features.

III. Result and Discussion

In this section, the results of the hardness and microstructural analysis of the fabricated walls using the WAAM process with ER70S-6 welding metal are presented and discussed. The primary objective was to assess the material consistency and mechanical properties of the walls through comprehensive hardness testing and microstructural examination. The analysis was conducted on a selected sample, which was chosen based on the highest tensile strength and maximum height, as detailed in the methodology section.

In this section of the hardness test, the hardness results at the highest point of the part were first examined, with a value of 204.1HV. As observed, the hardness in this section was higher than in the inner parts of the walls in horizontal lines. (Fig. 4).

This difference was due to rapid cooling processes in the outer layers, which were caused by heat transfer through convection with the surrounding air. In the outer sections of the part, this heat transfer occurred more rapidly, which led to an increase in hardness at the surface layers.

Rapid cooling in the outer layers of the part reduced the cooling time and, consequently, reduced the opportunity for grain growth in these layers. With rapid cooling, the grains in the outer layers became finer and more compact. Finer grains typically resulted in higher hardness, as the grain boundaries acted as barriers to the movement of dislocations. In other words, a greater number of grain boundaries meant that dislocations could not move as easily through the material, which increased resistance to deformation and, ultimately, increased hardness. Moreover, rapid cooling induced phase changes in the metal structure. In many alloys, such as steel, rapid cooling led to the formation of harder phases, such as martensite, which were harder than the austenitic or ferritic phases. In this study, rapid cooling in the outer layers of the wall reduced grain growth, resulting in finer grains and higher hardness. The increased grain boundary density impeded dislocation motion, thereby enhancing resistance to plastic deformation. Given that this point of the part was particularly important in machining processes, especially during the initial stages, hardness testing was performed at this location. In machining processes, work typically begins from the highest point of the part, as these points are of greater significance in terms of accessibility and thermal effects. Therefore, the hardness of the outer layers had a significant impact on the selection of machining parameters such as tool material, cutting speed, and other relevant variables. This was particularly important in determining optimal conditions to maintain surface quality and tool lifespan [35].

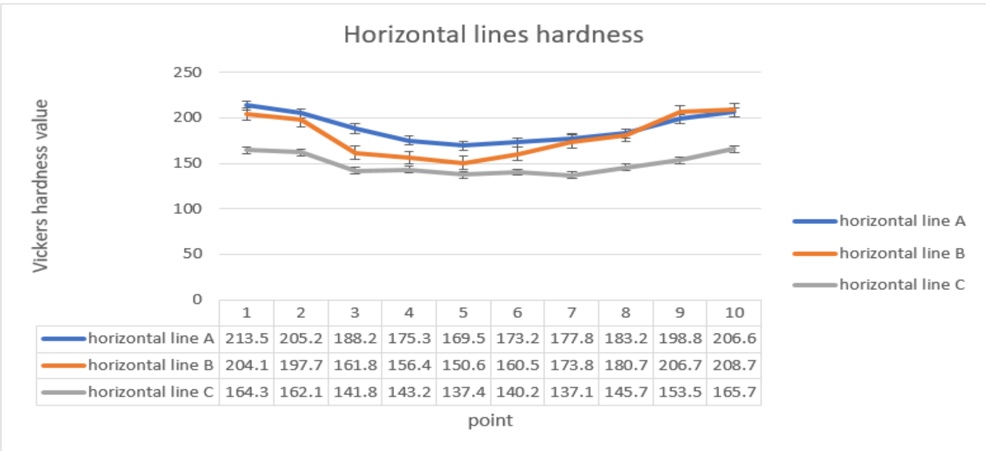

	1	2	3	4	5	6	7	8	9	10
horizontal line A	213.5	205.2	188.2	175.3	169.5	173.2	177.8	183.2	198.8	206.6
horizontal line B	204.1	197.7	161.8	156.4	150.6	160.5	173.8	180.7	206.7	208.7
horizontal line C	164.3	162.1	141.8	143.2	137.4	140.2	137.1	145.7	153.5	165.7

Fig. 4. Vickers hardness profile measured along horizontal lines A, B, and C across the WAAM-fabricated ER70S-6 wall

Hardness testing results revealed that the outer wall regions exhibited the highest hardness (approximately 200 HV), whereas the central region had the lowest hardness (around 160 HV). This variation in hardness significantly influences machining parameters and the final surface quality of the component. To better understand these effects, machining parameters for materials with similar hardness values were examined. AISI 1045 steel, with a hardness close to 213 HV, typically requires a cutting speed of 70-120 m/min, a feed rate of 0.1-0.25 mm/rev, and carbide cutting tools. For AISI 1018 steel, which has a hardness of approximately 180 HV, machining is generally performed at a cutting speed of 60-100 m/min with a feed rate of 0.15-0.3 mm/rev. In contrast, steels with 165 HV hardness, such as S235JR, require a lower cutting speed of 50-80 m/min, and high-speed steel (HSS) tools are more suitable for machining [36].

The final surface quality is heavily influenced by material hardness. Generally, harder materials produce smoother surfaces with lower roughness, as they are more resistant to plastic deformation and have a lower tendency to form built-up edges on cutting tools [37]. In the WAAM process, the gradual decrease in hardness from the wall edges toward the center can lead to higher surface roughness in the central regions [38]. Thus, machining parameters must be carefully controlled to ensure that softer layers are effectively removed, yielding a surface with the desired roughness and quality.

Additionally, machining parameters such as cutting speed, feed rate, and depth of cut have a direct impact on surface hardness and the final quality of the component. Increasing the cutting speed generally raises the temperature in the cutting zone, leading to microstructural changes in the surface layer. Moreover, feed rate and depth of cut significantly influence the residual stress distribution and surface roughness [39].

To achieve an optimal surface finish in WAAM-fabricated components, machining settings must be carefully adjusted to remove the lower-hardness layers, ensuring that the final surface has the desired hardness and roughness characteristics. Proper parameter selection not only enhances surface integrity but also improves the mechanical performance and wear resistance of the machined part.

In Fig. 3, the horizontal points were displayed, with lines namely A, B, and C representing the first, second, and third hardness test layers from the reference line. The results for the horizontal lines showed similar trends. In the first horizontal line (A), the hardness had started at 213.5 HV at point 1 (near the weld edge) and had decreased to 169.5 HV in the middle, reflecting a reduction of approximately 20.6%. The hardness then gradually increased, reaching 206.6 HV at the end of the line. In the second horizontal line (B), the hardness decreased from 204.1 HV at the initial point to 150.6 HV in the middle, showing a 26.2% reduction. By the end of the line, the hardness had increased to 208.7 HV. The third horizontal line (C) exhibited the most significant changes; the hardness started at 164.3 HV at the initial point, dropped to 137.4 HV in the middle (a 16.4% reduction), and then increased to 165.7 HV at the end. These changes indicated that near the weld edges, rapid cooling had led to finer grains and higher hardness [40]. In the middle of the lines, slower heat transfer allowed more time for grain growth, resulting in coarser grains and lower hardness [41]. Towards the substrate, faster cooling had again led to finer grains and increased hardness. Each of the 3 horizontal layers (A-A, B-B, C-C) in Fig. 3 had been analyzed separately, and the results highlighted the importance of weld edges, where the highest hardness values had been observed. This indicated that machining parameters needed to be adjusted based on the harder regions. Although the hardness values had decreased in the third line (C-C, this line was located in the central part of the sample and closer to the substrate, which had cooled more slowly), the higher hardness of the upper layers suggested that machining parameters should not have been based on the third line. Instead, the machining parameters needed to be selected based on the harder regions and remained consistent throughout the entire machining process.

Based on the results obtained from the microstructure images, in Fig. 5, a microstructure image of the center and edge of the wall fabricated using ER70S-6 filler metal was captured. The structure observed in the image represents a hypoeutectoid low-carbon steel. In the microstructure images, structures such as Axial Pearlite, Ferrite Grain, and Pearlite-Ferrite Mixture were observed. These specific microstructures were identified in different regions of the fabricated wall. The white and slightly darker regions are ferrite, while the black areas correspond to pearlite. Additionally, the ferrite grains are equiaxed. Furthermore, in this study, by employing scale calibration tools and image processing techniques of ImageJ software, the grain sizes in different regions of the specimen were determined. The results indicated that in areas near the wall, the grain size was smaller, leading to a higher grain count per unit area. Conversely, in the central regions of the specimen, the grain size was larger, resulting in a lower grain count within the same area.

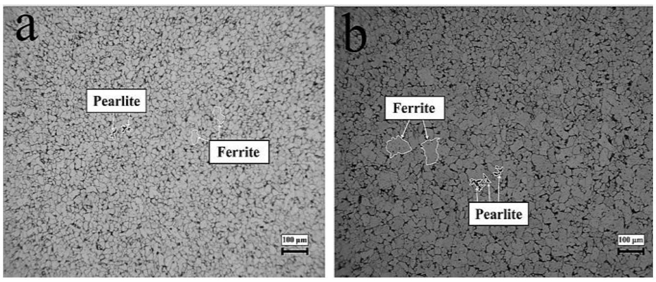

Fig. 5. Optical micrographs of the typical microstructures observed in MAG-WAAM fabricated ER70S-6 walls: (a) wall edges region, (b) wall central region

Furthermore, porosity was observed in the fabricated walls in Fig. 5, which is one of the most common defects in the WAAM process. Porosity can significantly reduce mechanical properties, such as strength and toughness. These defects appear as spherical or irregular voids distributed throughout the structure [42]. Porosity typically results from trapped gases during the melting and solidification process. The trapped gases may originate from shielding gas (e.g., CO_2 or argon), surface contaminants on the filler wire or substrate (e.g., oil, moisture, or oxides), or chemical reactions occurring during the process [42]. In cases of rapid solidification, the trapped gases do not have sufficient time to escape the molten pool, leading to microscopic voids in the final structure [42]. Areas with high thermal gradients are more prone to porosity formation, as rapid heat transfer prevents gas escape. Additionally, improper welding path design or insufficient overlap between layers can result in gas accumulation in localized regions [43].

In Fig. 6, SEM images illustrate distinct microstructural features within the MAG-WAAM fabricated wall of the low-carbon alloy ER70S6. The central region is dominated by a coarse, polygonal ferrite matrix accompanied by a secondary pearlite phase. These polygonal ferrite grains, with their well-defined, equiaxed boundaries, form as a result of slower cooling rates and the multiple thermal cycles inherent to the deposition process. Their evolution leads to a more homogeneous and ductile matrix, which may lower the yield strength while enhancing toughness. In contrast, the edge region, subject to more rapid cooling, exhibits a finer microstructure with acicular and polyghonal ferrite that contributes to increased strength. Additionally, several rounded or irregular voids are visible in the central region, likely resulting from trapped gas or incomplete fusion between layers.

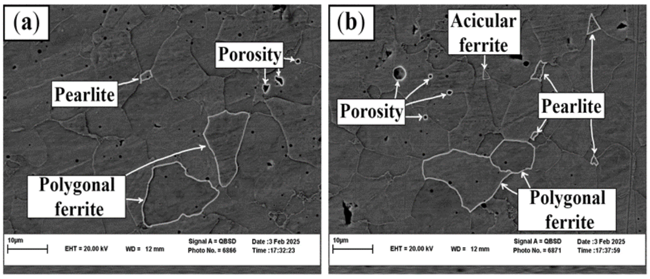

Fig. 6. SEM images of WAAM-fabricated ER70S-6 steel: (a) central region; (b) edge region

To minimize porosity in the WAAM process, precise control of process parameters is essential. This includes using high-quality materials free of contaminants, optimizing the flow of shielding gas to create a stable atmosphere, and managing the cooling rate effectively [44].

Although gas porosity can reduce the strength of the walls, the results of the strength tests show that, despite this defect, the strength of the walls fabricated using the WAAM method is still higher than the strength of the base ER70S-6 metal in most cases. This demonstrates the benefits and high potential of the WAAM method in producing components with improved mechanical properties, which can be particularly useful in industrial applications where there is a need for the production of complex parts with high strength.

The ER70S-6 electrodes typically consist of alloying elements that promote a ferritic structure. This ferritic structure resulted in fine grains in the wall regions and coarser grains in the central areas of the weld. The image confirms this distribution, with the ferritic and pearlitic phases forming a clear distinction in the material's microstructure. The finer grains in the walls are indicative of rapid cooling, while the coarser grains in the center result from slower heat transfer.

The welds fabricated with this material and structure exhibited distinct hardness distributions, with finer grains contributing to higher hardness values near the walls and coarser grains leading to reduced hardness in the middle. This variation in hardness distribution should be considered during the design and optimization of welding processes. It can also play a critical role in enhancing the overall mechanical strength of the welded part and improving its performance under various loading conditions. The observed microstructure emphasizes the importance of controlling cooling rates during the welding process to achieve desired mechanical properties.

IV. Conclusion

The hardness distribution in welded components plays a critical role in determining their mechanical properties and overall performance. This study examined the hardness variations across different regions of the weld to understand the effects of thermal cycles and microstructural changes during the WAAM process. The observed hardness trends were attributed to the interactions between heat input, cooling rates, and the resulting grain structures in various zones of the weld. Key findings regarding the hardness behavior and its implications are summarized below:

- Horizontal hardness values ranged from 164.3–213.5 HV at the weld edges to 137.4–169.5 HV in the middle regions, showing a ~20–25% decrease toward the center.
- Faster cooling near the edges and substrate produced finer ferritic–pearlitic grains, while slower cooling in the central zones led to coarser grain structures and lower hardness.
- Optical and SEM analyses confirmed a hypoeutectoid ferrite–pearlite microstructure, with equiaxed ferrite in the wall regions and polygonal ferrite with secondary pearlite in the center.
- Minor porosity was detected, attributed to trapped gases during solidification; however, it did not significantly reduce the overall tensile strength, which remained higher than that of the base ER70S-6 metal.
- The variation in hardness and microstructure emphasizes the need to control heat input and cooling rate to achieve uniform mechanical performance.
- The harder weld edges (up to ~209 HV) should be considered when defining machining parameters to ensure consistent surface quality and tool life.

Acknowledgment

The authors sincerely thank the Faculty of Engineering at Ferdowsi University for their generous support in granting access to the necessary facilities and laboratories for this research. They also extend their deep appreciation to the anonymous reviewers for their thoughtful feedback and constructive suggestions, which have significantly contributed to improving the quality of this work.

References

[1] J. Harrington Jr., “Understanding the Manufacturing Process: Key to Successful CAD/CAM Implementation,” *CRC Press*, 2020.

[2] S. Jung et al., "Is additive manufacturing an environmentally and economically preferred alternative for mass production?" *Environmental Science & Technology*, vol. 57, no. 16, pp. 6373–6386, 2023. https://doi.org/10.1021/acs.est.2c04927

[3] C. Maware et al., "Examining the progress in additive manufacturing in supporting lean, green and sustainable manufacturing: a systematic review," *Applied Sciences*, vol. 14, no. 14, p. 6041, 2024. https://doi.org/10.3390/app14146041

[4] M. Armstrong, H. Mehrabi, and N. Naveed, "An overview of modern metal additive manufacturing technology," *Journal of Manufacturing Processes*, vol. 84, pp. 1001–1029, 2022. https://doi.org/10.1016/j.jmapro.2022.10.060

[5] W. Huang et al., "Laser wire‑feed metal additive manufacturing of the Al alloy," *Optics & Laser Technology*, vol. 134, p. 106627, 2021. https://doi.org/10.1016/j.optlastec.2020.106627

[6] M. M. Imran et al., "Advancements in 3D printing: Directed energy deposition techniques, defect analysis, and quality monitoring," *Technologies*, vol. 12, no. 6, p. 86, 2024. https://doi.org/10.3390/technologies12060086

[7] R. Bidulsky et al., "Coated metal powders for laser powder bed fusion (L‑PBF) processing: a review," *Metals*, vol. 11, no. 11, p. 1831, 2021. https://doi.org/10.3390/met11111831

[8] M. Sivakumar et al., "Directed energy deposition (DED) process," in Advances in Additive Manufacturing, 2024, pp. 39–60. https://doi.org/10.1002/9781394238316.ch3

[9] S. Pattanayak and S. K. Sahoo, "Gas metal arc welding based additive manufacturing — a review," *CIRP Journal of Manufacturing Science and Technology*, vol. 33, pp. 398–442, 2021. https://doi.org/10.1016/j.cirpj.2021.04.010

[10] S. Kumar, N. S. Madugula, N. Kumar, and J. Giri, "An extensive analysis of GTAW process and its influence on the microstructure and mechanical properties of SDSS 2507," *Journal of Materials Research and Technology*, vol. 33, pp. 8675–8686, 2024. https://doi.org/10.1016/j.jmrt.2024.11.157

[11] M. Mazloom Farsibaf et al., "Micro‑size A‑TIG modeling and RSM optimization for enhanced AISI304L DOP," *Welding International*, vol. 39, no. 6, pp. 418–428, 2025. https://doi.org/10.1080/09507116.2025.2477012

[12] H. Zhang et al., "Investigating the influence mechanism of different shielding gas types on arc characteristics and weld quality in TA2 laser–arc hybrid welding," *Metals*, vol. 14, no. 8, p. 946, 2024. https://doi.org/10.3390/met14080946

[13] N. Kumar et al., "Wire arc additive manufacturing – a revolutionary method in additive manufacturing," *Materials Chemistry and Physics*, vol. 285, p. 126144, 2022. https://doi.org/10.1016/j.matchemphys.2022.126144

[14] T. N. Wordofa and P. J. Ramulu, "Gas metal arc welding input parameters impacts on weld quality characteristics of steel materials: a comprehensive exploration," *Technology*, vol. 3, no. 23, pp. 366–379, 2023. https://doi.org/10.21062/mft.2023.046

[15] J. Vora et al., "Experimental investigations on mechanical properties of multi-layered structure fabricated by GMAW-based WAAM of SS316L," *Journal of Materials Research and Technology*, vol. 20, pp. 2748–2757, 2022. https://doi.org/10.1016/j.jmrt.2022.08.074

[16] P. Shukla et al., "The influence of GMAW correction parameters on stabilizing the deposition characteristics for wire arc additive manufacturing," *Journal of Manufacturing Processes*, vol. 90, pp. 54–68, 2023. https://doi.org/10.1016/j.jmapro.2023.01.075

[17] C. Su et al., "Effect of heat input on microstructure and mechanical properties of Al‑Mg alloys fabricated by WAAM," *Applied Surface Science*, vol. 486, pp. 431–440, 2019. https://doi.org/10.1016/j.apsusc.2019.04.255

[18] M. Tongov et al., "Effect of heat input on microstructure and microhardness in WAAM," *Proceedings of the Bulgarian Academy of Sciences*, vol. 77, no. 9, pp. 1340–1346, 2024. https://doi.org/10.7546/CRABS.2024.09.09

[19] V. Nagallapati et al., "Active and passive thermal management in wire arc additive manufacturing," *Metals*, vol. 13, no. 4, p. 682, 2023. https://doi.org/10.3390/met13040682

[20] D. Fan et al., "Residual stress and microstructure properties by trailing cooling of argon gas of wire and arc additive manufacturing," *Journal of Manufacturing Processes*, vol. 77, pp. 32–39, 2022. https://doi.org/10.1016/j.jmapro.2022.03.007

[21] S. Panicker et al., "Investigation of thermal influence on weld microstructure and mechanical properties in wire and arc additive manufacturing of steels," *Materials Science and Engineering: A*, vol. 853, p. 143690, 2022. https://doi.org/10.1016/j.msea.2022.143690

[22] R. Scharf‑Wildenhain et al., "Heat control and design‑related effects on the properties and welding stresses in WAAM components of high‑strength structural steels," *Welding in the World*, vol. 67, no. 4, pp. 955–965, 2023. https://doi.org/10.1007/s40194-022-01450-x

[23] P. H. G. Dornelas et al., "Development of a gas metal arc based prototype for direct energy deposition with micrometric wire," *Journal of Materials Research and Technology*, vol. 30, pp. 3571–3583, 2024. https://doi.org/10.1016/j.jmrt.2024.04.056

[24] K. Ginjupalli and N. P. Upadhya, "Surface roughness of implants: A review," *Trends in Biomaterials and Artificial Organs*, vol. 25, no. 3, pp. 112–118, 2011.

[25] A. Chmielewska and D. Dean, "The role of stiffness‑matching in avoiding stress shielding‑induced bone loss and stress concentration‑induced skeletal reconstruction device failure," *Acta Biomaterialia*, vol. 173, pp. 51–65, 2024. https://doi.org/10.1016/j.actbio.2023.11.011

[26] A. Chmielewska and D. Dean, "The role of stiffness‑matching in avoiding stress shielding‑induced bone loss and stress concentration‑induced skeletal reconstruction device failure," *Acta Biomaterialia*, vol. 173, pp. 51–65, 2024. https://doi.org/10.1016/j.actbio.2023.11.011

[27] M. Dekis et al., "Unveiling the characteristics of ER70S‑6 low carbon steel alloy produced by wire arc additive manufacturing at different travel speeds," *Metals and Materials International*, vol. 31, no. 2, pp. 325–338, 2025. https://doi.org/10.1007/s12540-024-01766-x

[28] S. Saravanan et al., "Assessment of the tribological behavior of WAAM‑fabricated SS316L through advanced ensemble machine learning predictions and RSM‑based optimization," *Journal of Materials Engineering and Performance*, pp. 1–22, 2025. https://doi.org/10.1007/s11665-025-11691-8

[29] W. Zhai, N. Wu, and W. Zhou, "Effect of interpass temperature on wire arc additive manufacturing using high‑strength metal‑cored wire," *Metals*, vol. 12, no. 2, p. 212, 2022. https://doi.org/10.3390/met12020212

[30] A. A. Kardak and G. B. Sinclair, "Stress concentration factors for ASTM E8/E8M‑16a standard round specimens for tension testing," *Journal of Testing and Evaluation*, vol. 48, no. 1, pp. 711–719, 2020. https://doi.org/10.1520/JTE20190549

[31] X. Chen et al., "Microstructure and mechanical properties of the austenitic stainless steel 316L fabricated by gas metal arc additive manufacturing," *Materials Science and Engineering: A*, vol. 703, pp. 567–577, 2017. https://doi.org/10.1016/j.msea.2017.05.024

[32] M. Shamir et al., "Assessment of mechanical and fatigue crack growth properties of wire+arc additively manufactured mild steel components," *Fatigue & Fracture of Engineering Materials & Structures*, vol. 45, no. 10, pp. 2978–2989, 2022. https://doi.org/10.1111/ffe.13797

[33] M. G. Ganesh et al., "Investigation on mechanical properties of ER70S‑6 copper‑coated steel wire sample produced by wire arc additive manufacturing (WAAM)," In *International Conference on Trends in Automotive Parts Systems and Applications*, SAE Technical Paper, 2024.

[34] Y. Lu et al., "Comparative analysis of mechanical properties and microstructure of 7B52 aluminum alloy laser-MIG hybrid welding and MIG welding joints," *Metals*, vol. 14, no. 10, 2024. https://doi.org/10.3390/met14101110

[35] MM. Mukri et al., "Optimization of machining parameters in turning for different hardness using multi-objective genetic algorithm," *Journal of Mechanical Engineering (JMechE)*, vol. 20, no. 3, pp. 25-48, 2023. https://doi.org/10.24191/jmeche.v20i3.23899

[36] I.-S. Kang et al., "Influence of the material mechanical properties on cutting surface quality during turning," *Processes*, vol. 12, no. 6, p. 1171, 2024. https://doi.org/10.3390/pr12061171

[37] I. Basso et al., "Influences of the workpiece material and the tool-surface engagement (TSE) on surface finishing when ball-end milling," *Journal of Manufacturing Processes*, vol. 75, pp. 219-231, 2022. https://doi.org/10.1016/j.jmapro.2021.12.059

[38] O. C. Ozaner et al., "The influence of the wire and arc additive manufacturing parameters on the surface irregularities," *Journal of Micromanufacturing*, vol. 8, no. 1, 2024. https://doi.org/10.1177/25165984241306629

[39] S. Saini, I. S. Ahuja, and V. S. Sharma, "Residual stresses, surface roughness, and tool wear in hard turning: A comprehensive review," *Materials and Manufacturing Processes*, vol. 27, no. 6, pp. 583–598, 2012. https://doi.org/10.1080/10426914.2011.585505

[40] Y. Kalinin et al., "Structure of high‑carbon steel after welding with rapid cooling," *Acta Metallurgica Slovaca*, vol. 25, no. 2, pp. 114–122, 2019. https://doi.org/10.12776/ams.v25i2.1269

[41] S. Jeong et al., "Effect of line‑heating on the

microstructural and mechanical characteristics of 320‑MPa‑grade high‑strength hull plates," *Journal of Welding and Joining*, vol. 40, no. 4, pp. 352–357, 2022. https://doi.org/10.5781/JWJ.2022.40.4.8

[42] A. I. Albannai, "A brief review on the common defects in wire arc additive manufacturing," *International Journal of Current Science Research and Review*, vol. 5, pp. 4556–4576, 2022. https://doi.org/10.47191/ijcsrr/V5-i12-19

[43] K. L. M. Avegnon et al., "Porosity formation from disrupted gas flow in laser powder bed fusion of 316 stainless steel," *Journal of Manufacturing Processes*, vol. 90, pp. 333–340, 2023. https://doi.org/10.1016/j.jmapro.2022.12.032

[44] M. R. Zahidin et al., "Research challenges, quality control and monitoring strategy for wire arc additive manufacturing," *Journal of Materials Research and Technology*, vol. 24, pp. 2769–2794, 2023. https://doi.org/10.1016/j.jmrt.2023.03.200

[45] Y. Guo, "Microstructures and mechanical properties of ER70S‑6 steel fabricated by wire arc additive manufacturing," 2025.